

# Temperature tuned Fermi surface topology and segmentation in non-centrosymmetric superconductors

Madhuparna Karmakar<sup>1,2, \*</sup>

<sup>1</sup>Centre for Quantum Science and Technology, Chennai Institute of Technology, Chennai-600037, India.

<sup>2</sup>Department of Physics, Indian Institute of Technology, Madras, Chennai-600036, India.

(Dated: September 14, 2022)

We report the first comprehensive microscopic description of the thermal fluctuations tuned Fermi surface characteristics in a non-centrosymmetric superconductor, in presence of an in-plane Zeeman field. Using a non perturbative approach we demonstrate that short range fluctuating superconducting pair correlations give rise to segmentation of the Fermi surface with direction dependent pair breaking and hotspots for quasiparticle scattering. Further, a fluctuation driven change in the Fermi surface topology is realized, characterized by a shift of the corresponding Dirac point from the trivial  $\mathbf{k} = 0$  to the non trivial  $\mathbf{k} \neq 0$ . Our results provide key benchmarks for the thermal scales and regimes of thermal stability of these systems, that are important from the applied perspective to spintronic devices. Our theoretical estimates are in remarkable qualitative agreement with the recent differential conductance and quasiparticle interference measurements on  $\text{Bi}_2\text{Te}_3/\text{NbSe}_2$  hybrid. A generic theoretical framework for the finite momentum scattering of quasiparticles and the associated spectroscopic features is proposed, which is expected to be applicable to a wide class of superconducting materials.

**Introduction:** Intriguing superconducting (SC) phases are realized when the constraint of being equal and opposite in momentum is lifted off the pairing fermions. The key to break this constraint lies in lifting the spin degeneracy of the fermionic Bloch states, giving rise to spin-split Fermi surfaces (FS) [1]. The corresponding SC state responds to this non trivial FS by allowing the finite momentum ( $q$ ) scattering of the quasiparticles (QP). Experimental evidences of finite- $q$  scattering include, point contact spectroscopy showing gapless superconductivity [2] and anisotropic FS in rare earth quaternary borocarbides (RTBC) [3, 4], specific heat and magnetic torque measurements supporting Fulde-Ferrell-Larkin-Ovchinnikov (FFLO) superconductivity in two-dimensional (2D) organic superconductors [5–9], scanning tunneling spectroscopy in favor of in-gap states in magnet-superconductor hybrid (MSH) [10] and the very recent quasiparticle interference (QPI) measurements on non-centrosymmetric  $\text{Bi}_2\text{Te}_3/\text{NbSe}_2$  hybrid showing FS segmentation [11].

Non-centrosymmetric superconductors (NCS) and their response to in-plane Zeeman field have recently garnered interest [12–28] owing to the experimental observation of FS segmentation [11, 28] and SC diode effect [29–35] in these materials. QPI measurements on  $\text{Bi}_2\text{Te}_3/\text{NbSe}_2$  hybrid showed that the FS corresponding to the finite- $q$  paired state is segmented, with  $q$ -dependent isolated parts of the FS serving as hotspots for QP scattering [11]. In a similar spirit, magnetic field controlled SC diode effect has been observed in non-centrosymmetric artificial superlattice  $[\text{Nb}/\text{V}/\text{Ta}]_n$  [29]. Making use of the magnetochiral anisotropy (MA) of this material, a direction dependent zero resistance to the current flow was demonstrated [29]. The high temperature regime of such systems are shown to be immensely significant from the point of view of device applications. It was recently demonstrated that the performance of SC tunnel diode made up of  $\text{Cu}/\text{EuS}/\text{Al}$  tunnel junction is robust against thermal fluctuations upto a significantly high operating temperature, a prop-

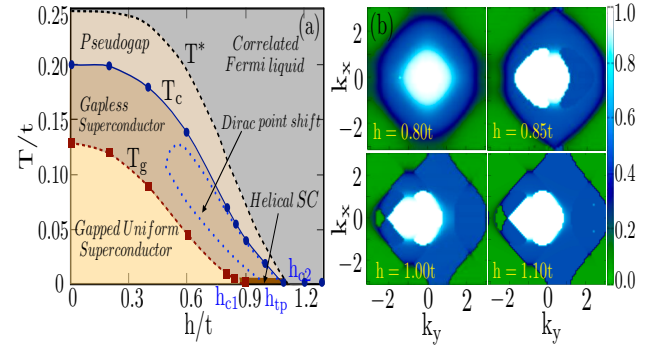


FIG. 1. (a) Thermal phase diagram in the  $h - T$  plane at  $\lambda = 0.65t$ , showing the thermal scales  $T_c$ ,  $T_g$  and  $T^*$ . The high temperature regime bounded by the dotted curves correspond to the fluctuation induced change in the FS topology, characterized by the shift in the Dirac point from  $\mathbf{k} = 0$  to  $\mathbf{k} \neq 0$ . (b) Evolution of FS topology with  $h$ , presented in terms of the fermionic occupation number  $n(\mathbf{k})$ . Note the single self intersecting FS at  $h = t$

erty that makes it appealing for electronic devices [36]. Similarly, magnetotransport measurements in the SC state of gated  $\text{MoS}_2$  demonstrated that the MA of this material is strongly dependent on temperature induced SC fluctuations and the ab-initio estimates of the MA parameter shows a discrepancy of five times w. r. t. the experimental observations [30]. These experiments suggest that the need of the hour is to have a theoretical understanding of the impact of thermal fluctuations on NCS.

Theoretical attempts to analyze the observations on NCSs have remained largely restricted to mean field theory (MFT) and perturbative approaches, which though are well suited to access the ground state properties, fail to capture the fluctuation effects [28, 31, 34, 37–40]. Access to thermal physics

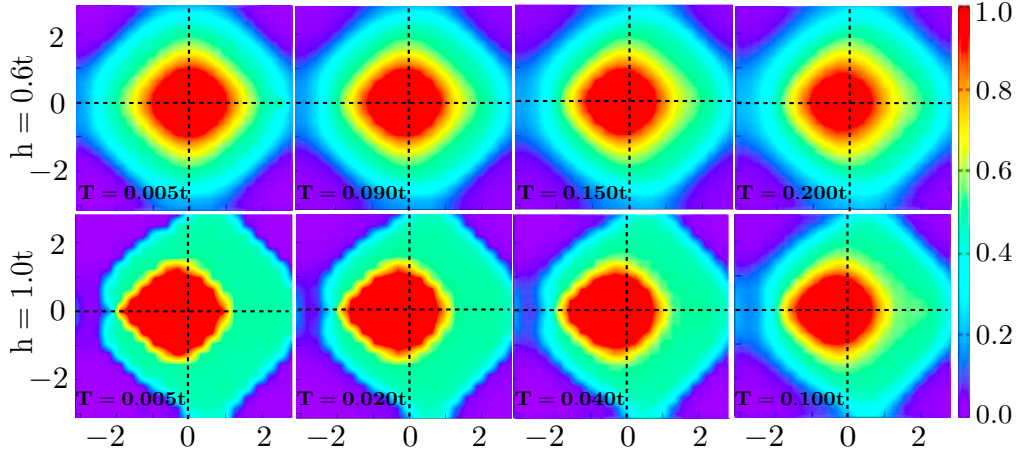


FIG. 2. Temperature dependence of FS topology at intermediate ( $h = 0.6t$ ) and strong ( $h = t$ ) Zeeman fields. The dashed lines are guide to the eyes for  $\mathbf{k} = 0$ . Note the self intersecting FS at  $T = 0.005t$  for  $h = t$ .

requires a beyond MFT approach to the problem and the complex parameter space with at least five competing energy scales viz. pairing interaction, spin-orbit coupling (SOC), Zeeman field, electron hopping and temperature, poses a computationally difficult problem.

In this letter we take a look at the 2D-NCS in the light of a non perturbative numerical approach that retains the spatial fluctuations of the SC pairing field at all orders. In particular, we investigate the finite temperature physics of this system in the space of competing pairing interaction ( $U$ ), SOC ( $\lambda$ ) and in-plane Zeeman field ( $h$ ), while retaining the temperature ( $T$ ) induced SC fluctuations. Our results provide estimates for the regime of thermal stability of the magnetochiral properties of these materials, which is important for spintronic devices.

Based on thermodynamic and spectroscopic signatures our key observations are as follows: (i) the system comprises of Zeeman field tuned two quantum critical points (QCP),  $h_{c1}$  and  $h_{c2}$ , corresponding to a first order phase transition, with a shift in the Dirac point to  $\mathbf{k} \neq 0$ , between the uniform and the helical SC (discussed later) phases, and a second order transition between the helical SC and a correlated Fermi liquid (CFL) phase, respectively. (ii) A topological transition (TT) of the FS takes place at  $h = h_{tp}$ , accompanied by a crossover between the interband and intraband paired helical SC phases. We note that the QCP  $h_{c1}$  is not tied to  $h_{tp}$  and no symmetry breaking takes place across the TT. (iii) Thermal fluctuations alter the FS topology and a temperature controlled shift of the Dirac point from the original  $\mathbf{k} = 0$  to  $\mathbf{k} \neq 0$  is realized for  $T \neq 0$ . (iv) FS segmentation takes place in the helical SC state, governed by thermal fluctuations generated hotspots for QP scattering. (v) Our results are in remarkable qualitative agreement with the experimental observations on  $\text{Bi}_2\text{Te}_3/\text{NbSe}_2$  hybrids [11]. The Zeeman field tuned evolution of the in-gap states as observed in differential conductance measurements as well as the FS segmentation observed

via QPI measurements on  $\text{Bi}_2\text{Te}_3/\text{NbSe}_2$  are well captured by our theoretical framework. Our results at  $T \neq 0$  are likely to trigger important high temperature experiments to realize thermally controlled MA in NCS.

*Model and observable:* Our starting Hamiltonian is the 2D attractive Hubbard model with Rashba spin-orbit coupling (RSOC) and in-plane Zeeman field [41–43],

$$\begin{aligned}
 H = & -t \sum_{\langle ij \rangle, \sigma} (c_{i,\sigma}^\dagger c_{j,\sigma} + h.c.) - \mu \sum_{i,\sigma} \hat{n}_{i,\sigma} - |U| \sum_i \hat{n}_{i,\uparrow} \hat{n}_{i,\downarrow} \\
 & + \lambda \sum_{ij,\sigma\sigma'} (c_{i,\sigma}^\dagger (i\hat{\sigma}_y)_{\sigma,\sigma'} c_{j,\sigma'} + c_{i,\sigma}^\dagger (-i\hat{\sigma}_x)_{\sigma,\sigma'} c_{j,\sigma'}) \\
 & + h \sum_i (c_{i,\uparrow}^\dagger c_{i,\downarrow} + c_{i,\downarrow}^\dagger c_{i,\uparrow})
 \end{aligned} \quad (1)$$

where,  $t = 1$  is the hopping amplitude between the nearest neighbors on a square lattice and sets the reference energy scale of the problem,  $\lambda$  is the magnitude of RSOC.  $|U| > 0$  is the on-site attractive interaction between the fermions and  $\mu$  is the global chemical potential which fixes the electron density. The in-plane Zeeman field ( $h$ ) is applied along the  $x$ -axis;  $\hat{\sigma}_x$  and  $\hat{\sigma}_y$  are the Pauli matrices.

The non-interacting ( $U = 0$ ) energy dispersion of Eq. 1 reads as,  $E_{\mathbf{k}}^\eta = \xi_{\mathbf{k}} \pm \sqrt{h^2 - 2ih\lambda \sin k_y - \lambda^2(\sin^2 k_x + \sin^2 k_y)}$ , where,  $\xi_{\mathbf{k}} = -2t(\cos k_x a + \cos k_y a) - \mu$  is the kinetic energy contribution, with lattice spacing  $a$ .  $E_{\mathbf{k}}^\eta$  corresponds to the helicity bands labeled by the helicity index  $\eta = \pm$ . In the limit of  $h = 0$ , the spectra comprises of four dispersion branches and with  $h \neq 0$  each branch splits into two [43]. We make the interacting ( $U \neq 0$ ) model numerically tractable via Hubbard Stratonovich (HS) decomposition of the quartic term [44, 45]. This introduces a complex scalar bosonic auxiliary field  $\Delta_i(\tau) = |\Delta_i(\tau)|e^{i\theta_i(\tau)}$  at each site, which couples to the SC pairing channel.

We address this problem using static path approximated

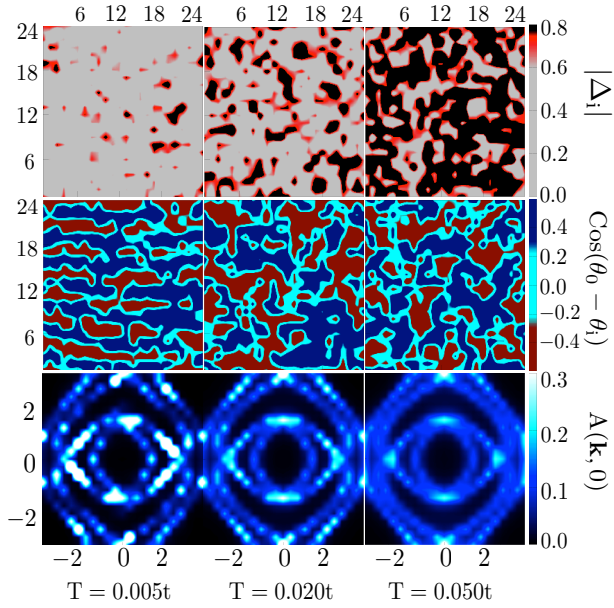


FIG. 3. Real space maps (in the  $xy$ -plane) corresponding to the SC pairing field amplitude,  $|\Delta_i|$  (top row) and SC phase coherence,  $\cos(\theta_0 - \theta_i)$  (middle row), showing the thermal evolution of the helical SC state at  $h = t$ . The bottom row maps out the segmented FS in terms of the low energy spectral weight distribution,  $A(\mathbf{k}, 0)$  (in the  $k_x, k_y$ -plane). Thermal fluctuations lead to fragmentation of the underlying SC state and progressive accumulation of spectral weight such that the FS isotropy is restored at  $T \sim 0.05t$ .

(SPA) quantum Monte Carlo technique, wherein we treat  $\Delta_i$  as classical by retaining its complete spatial fluctuations but taking into account only the  $\Omega_n = 0$  Matsubara mode in frequency (i. e.  $\Delta_i(\tau) \rightarrow \Delta_i$ ) [46–49] (see supplementary materials (SM)). The equilibrium configurations of  $\{\Delta_i\}$  (both for the uniform  $\mathbf{q} = 0$  and the helical  $\mathbf{q} \neq 0$  states) are generated via Monte Carlo (MC) simulation and the different fermionic correlators are computed on these equilibrium configurations. We verify our MC simulation results at the ground state using an alternate scheme of Bogoliubov-de-Gennes mean field theory (BdG-MFT).

We characterize the system based on the following indicators, (i) SC pairing field structure factor,  $S(\mathbf{q})$ , quantifying the (quasi) long range SC phase coherence; (ii) single particle density of states (DOS),  $N(\omega)$  and the corresponding spectral gap  $E_g$  at the Fermi level (zero energy); (iii) low energy spectral weight distribution,  $A(\mathbf{k}, 0)$ ; (iv) spectral function,  $A(\mathbf{k}, \omega)$  and (v) momentum resolved fermionic occupation number,  $n(\mathbf{k})$  (see SM). We work in the grand canonical ensemble with  $\mu = -t$  corresponding to an electron filling of  $n \approx 0.75$ , the pairing interaction is  $|U| = 4t$ . The simulations are carried out on a system size of  $L = 24$  (for MC) and of  $L = 70$  (for BdG-MFT), unless specified otherwise.

**Phase diagram and thermal scales:** Fig. 1(a) constitutes the primary result of this work, wherein we show the thermal

phase diagram of the 2D-NCS in the  $h$ – $T$  plane, for a selected RSOC of  $\lambda = 0.65t$ . The QCPs at  $h_{c1} \approx 0.85t$  and  $h_{c2} \approx 1.1t$ , correspond to a first order transition between gapped uniform ( $\mathbf{q} = 0$ ) and gapless helical ( $\mathbf{q} \neq 0$ ) SC phases and a second order transition between the helical SC and CFL, respectively. Within the helical SC phase the TT of the FS at  $h_{tp} \sim t$  is associated with a crossover between inter and intraband SC pairing. For  $h > h_{c2}$ , the SC correlations are lost.

The evolution of the FS topology across the QCPs is shown in Fig. 1(b) in terms of the fermionic occupation number  $n(\mathbf{k})$  at selected  $h$ .  $h = 0.80t$  is the representative of the  $0 < h \leq h_{c1}$  regime with uniform SC state. The corresponding concentric FSs are symmetric about the Dirac point at  $\mathbf{k} = 0$ .  $h = 0.85t$  represents the helical SC state in the regime  $h_{c1} < h \leq h_{tp}$  with the Dirac point shifted to  $\mathbf{k} \neq 0$ . At  $h_{tp} \sim t$ , the FSs cross each other giving rise to a *single self intersecting* FS akin to the Limacon of Pascal [37]. No quantum symmetry is broken across  $h_{tp}$  and this transition can't be detected via the routine spectroscopic and transport probes used to detect SC phase transitions. Further, increase in  $h$  decouples the FSs and pushes them apart, as shown at  $h = 1.1t$ . Note that the Dirac point is at  $\mathbf{k} \neq 0$  for the decoupled FSs and even at stronger  $h$  when the SC correlations are lost. The CFL containing FS with Dirac points at  $\mathbf{k} \neq 0$  is thus topologically different from the polarized Fermi liquid realized in the high magnetic field regime of FFLO [46] or the normal state of conventional and uniform superconductors.

The finite temperature phases are characterized by three thermal scales,  $T_c$ ,  $T_g$  and  $T^*$ , corresponding to the SC transition via the loss of global SC phase coherence, collapse of the zero energy SC spectral gap at the Fermi level and crossover between the pseudogap (PG) and CFL regimes, respectively. The thermal transition temperature  $T_c$  is determined based on the temperature dependence of  $S(\mathbf{q})$ , while the crossover scales  $T_g$  and  $T^*$  are determined based on the thermal evolution of  $N(\omega)$  at the Fermi level (see SM). The high temperature PG phase contains short range SC pair correlations, which show up as phase decohered SC islands. The regime is smoothly connected to the CFL via gradual degradation of the short range SC pair correlations.

**Temperature tuned FS topology:** Thermal fluctuations induced short range SC correlations alter the FS topology over the regime enveloped by the dotted curves, in Fig. 1(a). We understand this behavior based on Fig. 2, which shows the thermal evolution of the FS at selected Zeeman field of  $h = 0.6t$  and  $h = t$ . At  $h = 0.6t$ , the low temperature phase ( $T \leq 0.04t$ ) corresponds to a gapped uniform superconductor, with the Dirac point at  $\mathbf{k} = 0$ , followed by a gapless SC regime  $0.04t < T \leq 0.15t$ . Within the gapless phase, temperature alters the FS topology by progressively shifting the Dirac point from  $\mathbf{k} = 0$  to  $\mathbf{k} \neq 0$  over the regime  $0.09t < T \leq 0.15t$ , indicating the dominance of fluctuation induced helical SC correlations. The FS undergoes fluctuation induced broadening in the PG regime,  $T > T_c = 0.15t$ .

At  $h = t$ , the system is in the helical SC state with a single self intersecting FS, as shown at  $T = 0.005t$ . Temperature de-

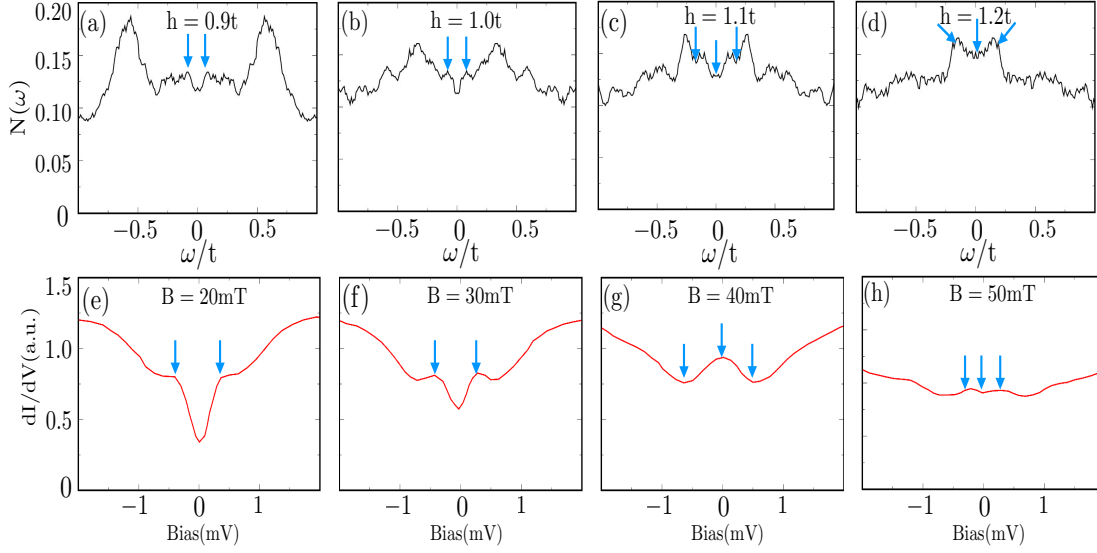


FIG. 4. Comparison of the evolution of the in-gap states with Zeeman field in the helical SC phase with the experimental observations on  $\text{Bi}_2\text{Te}_3/\text{NbSe}_2$  hybrid [11]. The top panels correspond to the theoretically computed single particle DOS as function of the Zeeman field and the bottom panels show the results obtained via differential conductance measurement in  $\text{Bi}_2\text{Te}_3/\text{NbSe}_2$  hybrid, as function of the applied magnetic field  $B||\Gamma - M$  [11]. The arrows indicate the in-gap states.

couples the FSs and progressively shifts the smaller FS away from the edge of the larger, over the regime  $0 < T \leq 0.02t$ . This thermal fluctuations driven transition of the FS topology is accompanied by the crossover between intra and interband helical SC correlations. Loss of local SC correlations for  $T > 0.04t$  is indicated by the broadening of the FS.

*Helical superconductivity and Fermi surface segmentation:* We next analyze the helical SC state in terms of its real and momentum space characteristics. Fig.3 shows the temperature dependence of the SC pairing field amplitude ( $|\Delta_i|$ ) (top row) and phase coherence ( $\cos(\theta_0 - \theta_i)$ ) (middle row). The low temperature helical SC phase is characterized by a spatially uniform SC amplitude and a one dimensional (1D) modulated phase coherence. Fluctuations progressively destroys the global SC order via loss of (quasi) long range phase coherence. The state undergoes spatial fragmentation into phase decohered islands with large local pairing field amplitude, corresponding to the PG phase.

The bottom row of Fig.3 shows the segmentation of the FS, mapped out in terms of the low energy spectral weight distribution  $A(\mathbf{k}, 0)$ . Finite- $q$  pairing leads to direction dependent pair breaking, such that only parts of the gapless FS are available for the scattering of the QPs. Temperature leads to the accumulation of spectral weight such that the FS isotropy is restored for  $T \geq 0.05t$ . Our results at low temperatures, shown in Fig.3 are in remarkable agreement with the experimental observations on  $\text{Bi}_2\text{Te}_3/\text{NbSe}_2$  hybrid [11]. QPI measurements on this NCS showed FS segmentation with  $q$ -dependent QP scattering. The corresponding real space behavior, as established via differential conductance maps show 1D standing

wave modulations [11], akin to our results in Fig.3.

*Comparison with experiment and finite energy pairing:* We now compare in Fig.4, our low temperature single particle DOS ( $N(\omega)$ ) at different Zeeman fields with the differential conductance measurement on  $\text{Bi}_2\text{Te}_3/\text{NbSe}_2$  hybrid [11]. In consonance with the experimental observation, the  $N(\omega)$  exhibits Zeeman field tuned evolution of the in-gap states. We understand this as follows: owing to the finite- $q$  pairing the  $|\mathbf{k}_\uparrow\rangle$  state not just connects with  $|\mathbf{k}_\downarrow\rangle$ , but with  $|\mathbf{k} + \mathbf{q}_\uparrow\rangle$  and  $|\mathbf{k} - \mathbf{q}_\downarrow\rangle$  states as well. The resulting dispersion spectra contains multiple branches and gives rise to additional van Hove singularities, which shows up as in-gap states in  $N(\omega)$ .

We understand this physics using Fig.5 where we show the systematic evolution of the low temperature spectroscopic properties of this system across the QCPs. At  $h = 0$ , the dispersion spectra of the  $s$ -wave NCS contains four branches, as shown via the  $A(\mathbf{k}, \omega)$  map. The uniform SC state is interband paired with fermions belonging to the two helicity bands pairing up. The corresponding spectra is gapped at the zero energy with sharp van Hove singularities at the gap edges, indicating the (quasi) long range SC phase coherence. Zeeman field ( $h = 0.6t$ ) splits the dispersion branches, the spectral gap at the zero energy arising from the uniform interband pairing is suppressed in magnitude. Additional finite energy “shadow gaps” open up, which are symmetrically located at  $\omega \approx \pm U/2$ . These shadow gaps which are the replicas of the zero energy gap and recently discussed in the context of Ising superconductors [50], arises out of the intraband uniform pairing in the individual helicity bands. Thus, the intermediate  $0 < h \leq h_{c1}$  regime contains SC state with admixture of uniform inter and



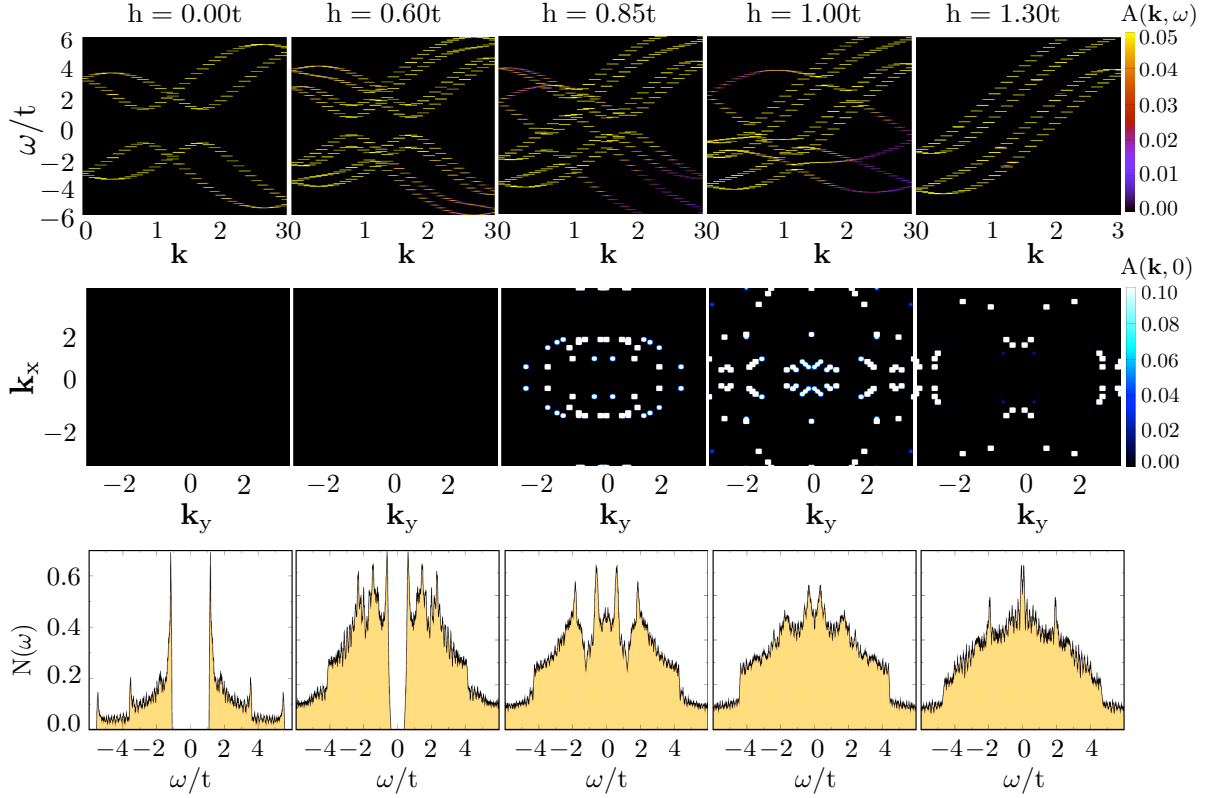


FIG. 5. Spectroscopic properties, (i) spectral function,  $A(\mathbf{k}, \omega)$  (top row), (ii) low energy spectral weight distribution,  $A(\mathbf{k}, 0)$  (middle row) and (iii) single particle DOS,  $N(\omega)$  (bottom row), at the ground state as function of  $h$ , determined using BdG-MFT for  $L = 70$ . For  $h = 0$  uniform interband superconductivity is realized between the helicity bands, giving rise to a robust zero energy SC gap. The corresponding  $A(\mathbf{k}, 0)$  is featureless and  $N(\omega)$  shows prominent gap edge singularities.  $h \neq 0$  splits the helicity bands, allows for symmetric finite energy intraband SC pairing and opens up the corresponding shadow gaps. For  $h > h_{c1}$  the system is in the helical SC state and the multi-branched dispersion gives rise to gapless spectra. The corresponding  $N(\omega)$  has finite spectral weight at the Fermi level and in-gap states. The FS is segmented, as observed via  $A(\mathbf{k}, 0)$ , with isolated hotspots for quasiparticle scattering. The strong  $h$  regime ( $h > h_{c2}$ ) corresponds to the CFL phase with anisotropic FS akin to a magnetic metal.

intraband pairing. In this regime the multiple branches of the dispersion spectra arises out of the interplay of SOC and in-plane Zeeman field, and doesn't involve any finite- $q$  scattering of the QPs. Expectedly, the SC pairing continues to be between the  $|\mathbf{k}_\uparrow\rangle$  and the  $|\mathbf{k}_\downarrow\rangle$  states and there are no FS segmentation and in-gap states either in the zero or in the finite energy SC gaps.

The helical SC phase ( $h = 0.85t$ ) with finite- $q$  pairing contains multiple dispersion branches which connects a larger set of states. Some of these dispersion branches crosses the Fermi level, giving rise to gapless superconductivity. SC pairing is interband in the regime  $h_{c1} < h \leq h_{ip}$  and the shadow gaps are strongly suppressed. Note that a recent MFT study have discussed the possibility of finite energy finite momentum pairing in Fulde-Ferrell (FF) superconductors, in the absence of RSOC [51]. The FS of the helical SC state is segmented with direction dependent pair breaking, as shown via ( $A(\mathbf{k}, 0)$ ). The crossing of the dispersion branches (as observed in  $A(\mathbf{k}, \omega)$ ) give rise to the additional van Hove sin-

gularities and the associated in-gap states, as observed in the corresponding  $N(\omega)$ . At  $h = h_{ip} = t$ , a single self intersecting FS is realized which is reflected in  $A(\mathbf{k}, \omega)$  as self intersecting dispersion branches. The corresponding SC state undergoes topological transition from the inter to the intraband pairing and continues to be an intraband helical superconductor over the regime  $h_{ip} < h \leq h_{c2}$ . SC correlations are lost at  $h = 1.3t$  and the dispersion spectra is akin to that of a magnetic metal with anisotropic FS.

*Discussion and conclusions:* Segmentation of FS and multibranch dispersion are generic properties associated with finite- $q$  scattering of QPs. The helical SC state constitutes one of the examples, while the others include FFLO [5–9, 46, 52–56], MSH [10, 57, 58], magnetic superconductors such as, RTBC [3, 4, 59–62] etc. Our analysis of the SC state based on Fig.5 is generic and is applicable to other systems as well. Gapless SC phase with anisotropic (nodal) FS has been experimentally observed in  $\text{YNi}_2\text{B}_2\text{C}$  and  $\text{LuNi}_2\text{B}_2\text{C}$  [63–67], and magnetic fluctuations were proposed to play a key role in

defining the FS and SC gap architecture in these [59] and related class of materials [60, 61].

In a similar spirit, Nuclear magnetic resonance (NMR) measurements on 2D organic superconductor  $\beta''$ -(BEDT-TTF)<sub>2</sub>SF<sub>5</sub>CH<sub>2</sub>CF<sub>2</sub>SO<sub>3</sub> (BEDT-TTF) showed that the high magnetic field low temperature regime hosts FFLO state with 1D modulated SC order [9]. de Hass-van Alphen measurements and angle dependent magnetoresistance oscillations were utilized to map out the highly anisotropic 2D FS of BEDT-TTF [6]. Theoretically, a non perturbative beyond MFT study of the FFLO phase in an isotropic *s*-wave superconductor established FS segmentation, in terms of the spectroscopic signatures [56]. Thus, irrespective of its origin, finite-*q* scattering of QPs bring out similar physics in widely different classes of SC systems.

In conclusion, based on a non perturbative numerical approach we have investigated the spin split non-centrosymmetric superconductor in presence of an in-plane Zeeman field. In the complex parameter space of SC interaction, RSOC, Zeeman field and temperature we showed that thermal fluctuations alter the FS topology and shifts the corresponding Dirac point from  $\mathbf{k} = 0$  to  $\mathbf{k} \neq 0$ . Further, we established that a temperature controlled FS segmentation is realizable in these systems, such that only parts of the FS serves as hotspots for quasiparticle scattering. The response of the SC state to the Zeeman field is analyzed based of the spectroscopic and thermodynamic signatures and the regimes of different SC pairings are mapped out. The results presented in this letter provide benchmarks for the thermal scales and regime of stability of these systems against thermal fluctuations, which are important from the perspective of spintronic devices. Our results are compared with the experimental observations on Bi<sub>2</sub>Te<sub>3</sub>/NbSe<sub>2</sub> hybrid and are found to be in remarkable qualitative agreement. It is expected that the results discussed in this letter will trigger important experiments to capture the temperature controlled properties of NCS and their response to in-plane Zeeman field. A generic theoretical framework for finite momentum scattering of quasiparticles and the associated FS signatures is provided, which should be applicable to a wide class of SC materials.

**Acknowledgement:** The author acknowledges the use of the high performance computing cluster facility (AQUA) at IIT Madras, India. Funding from the Center for Quantum Information Theory in Matter and Spacetime, IIT Madras is acknowledged. The author would like to thank Avijit Misra for the critical reading of the manuscript.

---

\* madhuparna.k@gmail.com

- [1] R. Meservey and P.M. Tedrow, “Spin-polarized electron tunneling,” *Physics Reports* **238**, 173–243 (1994).
- [2] L.F. Rybaltchenko, A.G.M. Jansen, P. Wyder, L.V. Tjutrina, P.C. Canfield, C.V. Tomy, and D.McK. Paul, “Point-contact study of the magnetic superconductor HoNi<sub>2</sub>B<sub>2</sub>C,” *Physica C: Superconductivity* **319**, 189–196 (1999).
- [3] T. Baba, T. Yokoya, S. Tsuda, T. Kiss, T. Shimojima, K. Ishizaka, H. Takeya, K. Hirata, T. Watanabe, M. Nohara, H. Takagi, N. Nakai, K. Machida, T. Togashi, S. Watanabe, X.-Y. Wang, C. T. Chen, and S. Shin, “Bulk electronic structure of the antiferromagnetic superconducting phase in ErNi<sub>2</sub>B<sub>2</sub>C,” *Phys. Rev. Lett.* **100**, 017003 (2008).
- [4] M. Schneider, G. Fuchs, K.-H. Müller, K. Nenkov, G. Behr, D. Souptel, and S.-L. Drechsler, “Magnetic pair breaking in superconducting HoNi<sub>2</sub>B<sub>2</sub>C studied on a single crystal by thermal conductivity in magnetic fields,” *Phys. Rev. B* **80**, 224522 (2009).
- [5] R. Beyer, B. Bergk, S. Yasin, J. A. Schlueter, and J. Wosnitza, “Angle-dependent evolution of the fulde-ferrell-larkin-ovchinnikov state in an organic superconductor,” *Phys. Rev. Lett.* **109**, 027003 (2012).
- [6] J. Wosnitza, S. Wanka, J.S. Qualls, J.S. Brooks, C.H. Mielke, N. Harrison, J.A. Schlueter, J.M. Williamsd, P.G. Nixon, R.W. Winter, and G.L. Gard, “Fermiology of the organic superconductor  $\beta''$ -(ET)<sub>2</sub>SF<sub>5</sub>CH<sub>2</sub>CF<sub>2</sub>SO<sub>3</sub>,” *Synthetic Metals* **103**, 2000–2001 (1999).
- [7] J. A. Wright, E. Green, P. Kuhns, A. Reyes, J. Brooks, J. Schlueter, R. Kato, H. Yamamoto, M. Kobayashi, and S. E. Brown, “Zeeman-driven phase transition within the superconducting state of  $\kappa$ -(BEDT-TTF)<sub>2</sub>Cu(NCS)<sub>2</sub>,” *Phys. Rev. Lett.* **107**, 087002 (2011).
- [8] H. Mayaffre, S. Krämer, M. Horvatić, C. Berthier, K. Miyagawa, K. Kanoda, and V. F. Mitrovic, “Evidence of andreev bound states as a hallmark of the fflo phase in  $\kappa$ -(BEDT-TTF)<sub>2</sub>Cu(NCS)<sub>2</sub>,” *Nature Physics* **10**, 928 (2014).
- [9] G. Koutroulakis, H. Kühne, J. A. Schlueter, J. Wosnitza, and S. E. Brown, “Microscopic study of the fulde-ferrell-larkin-ovchinnikov state in an all-organic superconductor,” *Phys. Rev. Lett.* **116**, 067003 (2016).
- [10] Roberto Lo Conte, Maciej Bazarnik, Krisztián Palotás, Levente Rózsa, László Szunyogh, André Kubetzka, Kirsten von Bergmann, and Roland Wiesendanger, “Coexistence of antiferromagnetism and superconductivity in Mn/Nb(110),” *Phys. Rev. B* **105**, L100406 (2022).
- [11] Zhen Zhu, Michal Papaj, Xiao-Ang Nie, Hao-Ke Xu, Yi-Sheng Gu, Xu Yang, Dandan Guan, Shiyong Wang, Yaoyi Li, Canhua Liu, Jianlin Luo, Zhu-An Xu, Hao Zheng, Liang Fu, and Jin-Feng Jia, “Discovery of segmented fermi surface induced by cooper pair momentum,” *Science* **374**, 1381–1385 (2021).
- [12] Liang Fu and C. L. Kane, “Superconducting proximity effect and majorana fermions at the surface of a topological insulator,” *Phys. Rev. Lett.* **100**, 096407 (2008).
- [13] Jason Alicea, “Majorana fermions in a tunable semiconductor device,” *Phys. Rev. B* **81**, 125318 (2010).
- [14] Yuval Oreg, Gil Refael, and Felix von Oppen, “Helical liquids and majorana bound states in quantum wires,” *Phys. Rev. Lett.* **105**, 177002 (2010).
- [15] Roman M. Lutchyn, Jay D. Sau, and S. Das Sarma, “Majorana fermions and a topological phase transition in semiconductor-superconductor heterostructures,” *Phys. Rev. Lett.* **105**, 077001 (2010).
- [16] Andrew C. Potter and Patrick A. Lee, “Majorana end states in multiband microstructures with rashba spin-orbit coupling,” *Phys. Rev. B* **83**, 094525 (2011).
- [17] V. Mourik, K. Zuo, S. M. Frolov, S. R. Plissard, E. P. A. M. Bakkers, and L. P. Kouwenhoven, “Signatures of majorana fermions in hybrid superconductor-semiconductor nanowire devices,” *Science* **336**, 1003–1007 (2012).
- [18] Anindya Das, Yuval Ronen, Yonatan Most, Yuval Oreg, Moty Heiblum, and Hadas Shtrikman, “Zero-bias peaks and splitting

- in an al-inas nanowire topological superconductor as a signature of majorana fermions,” *Nature Physics* **8**, 887 (2012).
- [19] Hao-Hua Sun, Kai-Wen Zhang, Lun-Hui Hu, Chuang Li, Guan-Yong Wang, Hai-Yang Ma, Zhu-An Xu, Chun-Lei Gao, Dan-Dan Guan, Yao-Yi Li, Canhua Liu, Dong Qian, Yi Zhou, Liang Fu, Shao-Chun Li, Fu-Chun Zhang, and Jin-Feng Jia, “Majorana zero mode detected with spin selective andreev reflection in the vortex of a topological superconductor,” *Phys. Rev. Lett.* **116**, 257003 (2016).
  - [20] J. M. Lu, O. Zheliuk, I. Leermakers, N. F. Q. Yuan, U. Zeitler, K. T. Law, and J. T. Ye, “Evidence for two-dimensional ising superconductivity in gated MoS<sub>2</sub>,” *Science* **350**, 1353–1357 (2015).
  - [21] Yu Saito, Yasuharu Nakamura, Mohammad Saeed Bahramy, Yoshimitsu Kohama, Jianting Ye, Yuichi Kasahara, Yuji Nakagawa, Masaru Onga, Masashi Tokunaga, Tsutomu Nojima, Youichi Yanase, and Yoshihiro Iwasa, “Superconductivity protected by spin–valley locking in ion-gated MoS<sub>2</sub>,” *Nature Physics* **12**, 144 (2016).
  - [22] Xiaoxiang Xi, Zefang Wang, Weiwei Zhao, Ju-Hyun Park, Kam Tuen Law, Helmuth Berger, László Forró, Jie Shan, and Kin Fai Mak, “Ising pairing in superconducting NbSe<sub>2</sub> atomic layers,” *Nature Physics* **12**, 139 (2016).
  - [23] Benjamin T. Zhou, Noah F. Q. Yuan, Hong-Liang Jiang, and K. T. Law, “Ising superconductivity and majorana fermions in transition-metal dichalcogenides,” *Phys. Rev. B* **93**, 180501 (2016).
  - [24] Liang Fu and Erez Berg, “Odd-parity topological superconductors: Theory and application to Cu<sub>x</sub>Bi<sub>2</sub>Se<sub>3</sub>,” *Phys. Rev. Lett.* **105**, 097001 (2010).
  - [25] Sho Nakosai, Yukio Tanaka, and Naoto Nagaosa, “Topological superconductivity in bilayer rashba system,” *Phys. Rev. Lett.* **108**, 147003 (2012).
  - [26] Vladyslav Kozii and Liang Fu, “Odd-parity superconductivity in the vicinity of inversion symmetry breaking in spin-orbit-coupled systems,” *Phys. Rev. Lett.* **115**, 207002 (2015).
  - [27] Fengcheng Wu and Ivar Martin, “Nematic and chiral superconductivity induced by odd-parity fluctuations,” *Phys. Rev. B* **96**, 144504 (2017).
  - [28] Noah F. Q. Yuan and Liang Fu, “Zeeman-induced gapless superconductivity with a partial fermi surface,” *Phys. Rev. B* **97**, 115139 (2018).
  - [29] Fuyuki Ando, Yuta Miyasaka, Tian Li, Jun Ishizuka, Tomonori Arakawa, Yoichi Shiota, Takahiro Moriyama, Youichi Yanase, and Teruo Ono, “Observation of superconducting diode effect,” *Nature* **584**, 373 (2020).
  - [30] Ryohei Wakatsuki, Yu Saito, Shintaro Hoshino, Yuki M. Itahashi, Toshiya Ideue, Motohiko Ezawa, Yoshihiro Iwasa, and Naoto Nagaosa, “Nonreciprocal charge transport in noncentrosymmetric superconductors,” *Science Advances* **3**, e1602390 (2017).
  - [31] Akito Daido, Yuhei Ikeda, and Youichi Yanase, “Intrinsic superconducting diode effect,” *Phys. Rev. Lett.* **128**, 037001 (2022).
  - [32] James Jun He, Yukio Tanaka, and Naoto Nagaosa, “A phenomenological theory of superconductor diodes,” *New Journal of Physics* **24**, 053014 (2022).
  - [33] Ryohei Wakatsuki and Naoto Nagaosa, “Nonreciprocal current in noncentrosymmetric rashba superconductors,” *Phys. Rev. Lett.* **121**, 026601 (2018).
  - [34] Noah F. Q. Yuan and Liang Fu, “Supercurrent diode effect and finite-momentum superconductors,” *Proceedings of the National Academy of Sciences* **119**, e2119548119 (2022).
  - [35] Yi Zhang, Yuhao Gu, Jiangping Hu, and Kun Jiang, “General theory of josephson diodes,” (2021), 10.48550/ARXIV.2112.08901.
  - [36] E. Strambini, M. Spies, N. Ligato, S. Ilić, M. Rouco, Carmen González-Orellana, Maxim Ilyn, Celia Rogero, F. S. Bergeret, J. S. Moodera, P. Virtanen, T. T. Heikkilä, and F. Giazotto, “Superconducting spintronic tunnel diode,” *Nature Communications* **13**, 2431 (2022).
  - [37] Noah F. Q. Yuan and Liang Fu, “Topological metals and finite-momentum superconductors,” *Proceedings of the National Academy of Sciences* **118**, e2019063118 (2021).
  - [38] Alireza Akbari and Peter Thalmeier, “Fermi surface segmentation in the helical state of a rashba superconductor,” *Phys. Rev. Research* **4**, 023096 (2022).
  - [39] Peter Thalmeier and Alireza Akbari, “Dynamical magnetic response in superconductors with finite momentum pairs,” (2022), 10.48550/ARXIV.2205.09207.
  - [40] Michał Papaj and Liang Fu, “Creating majorana modes from segmented fermi surface,” *Nature Communications* **12**, 577 (2021).
  - [41] Yong Xu, Chunlei Qu, Ming Gong, and Chuanwei Zhang, “Competing superfluid orders in spin-orbit-coupled fermionic cold-atom optical lattices,” *Phys. Rev. A* **89**, 013607 (2014).
  - [42] Fan Wu, Guang-Can Guo, Wei Zhang, and Wei Yi, “Unconventional superfluid in a two-dimensional fermi gas with anisotropic spin-orbit coupling and zeeman fields,” *Phys. Rev. Lett.* **110**, 110401 (2013).
  - [43] M. Smidman, M. B. Salamon, H. Q. Yuan, and D. F. Agterberg, “Superconductivity and spin–orbit coupling in non-centrosymmetric materials: a review,” *Reports on Progress in Physics* **80**, 036501 (2017).
  - [44] J. Hubbard, “Calculation of partition functions,” *Phys. Rev. Lett.* **3**, 77–78 (1959).
  - [45] H. J. Schulz, “Effective action for strongly correlated fermions from functional integrals,” *Phys. Rev. Lett.* **65**, 2462–2465 (1990).
  - [46] Madhuparna Karmakar and Pinaki Majumdar, “Population-imbalanced lattice fermions near the BCS–BEC crossover: Thermal physics of the breached pair and Fulde–Ferrell–Larkin–Ovchinnikov phases,” *Phys. Rev. A* **93**, 053609 (2016).
  - [47] Madhuparna Karmakar, “Thermal transitions, pseudogap behavior, and BCS–BEC crossover in Fermi–Fermi mixtures,” *Phys. Rev. A* **97**, 033617 (2018).
  - [48] Madhuparna Karmakar, “Pauli limited d-wave superconductors: quantum breached pair phase and thermal transitions,” *Journal of Physics: Condensed Matter* **32**, 405604 (2020).
  - [49] Nyayabanta Swain and Madhuparna Karmakar, “Strain-induced superconductor-insulator transition on a lieb lattice,” *Phys. Rev. Research* **2**, 023136 (2020).
  - [50] Gaomin Tang, Christoph Bruder, and Wolfgang Belzig, “Magnetic field-induced “mirage” gap in an ising superconductor,” *Phys. Rev. Lett.* **126**, 237001 (2021).
  - [51] Debmalya Chakraborty and Annica M. Black-Schaffer, “Interplay of finite-energy and finite-momentum superconducting pairing,” *Phys. Rev. B* **106**, 024511 (2022).
  - [52] T. K. Koponen, T. Paananen, J.-P. Martikainen, and P. Törmä, “Finite-temperature phase diagram of a polarized fermi gas in an optical lattice,” *Phys. Rev. Lett.* **99**, 120403 (2007).
  - [53] M. J. Wolak, B. Grémaud, R. T. Scalettar, and G. G. Batrouni, “Pairing in a two-dimensional fermi gas with population imbalance,” *Phys. Rev. A* **86**, 023630 (2012).
  - [54] Miikka O. J. Heikkinen, Dong-Hee Kim, and Päivi Törmä, “Finite-temperature stability and dimensional crossover of exotic superfluidity in lattices,” *Phys. Rev. B* **87**, 224513 (2013).

- [55] M. O. J. Heikkinen, D.-H. Kim, M. Troyer, and P. Törmä, “Nonlocal quantum fluctuations and fermionic superfluidity in the imbalanced attractive hubbard model,” *Phys. Rev. Lett.* **113**, 185301 (2014).
- [56] Madhuparna Karmakar, “Imbalanced fermi systems and exotic superconducting phases,” (2020), 10.48550/ARXIV.2008.11740.
- [57] Stefan Rex, Igor V. Gornyi, and Alexander D. Mirlin, “Majorana bound states in magnetic skyrmions imposed onto a superconductor,” *Phys. Rev. B* **100**, 064504 (2019).
- [58] Guang Yang, Peter Stano, Jelena Klinovaja, and Daniel Loss, “Majorana bound states in magnetic skyrmions,” *Phys. Rev. B* **93**, 224505 (2016).
- [59] Hiroshi Kontani, “Theory of anisotropic  $s$ -wave superconductivity with point-node-like gap minima: Analysis of (Y,Lu)Ni<sub>2</sub>B<sub>2</sub>C,” *Phys. Rev. B* **70**, 054507 (2004).
- [60] Madhuparna Karmakar and Pinaki Majumdar, “Noncollinear order and gapless superconductivity in  $s$ -wave magnetic superconductors,” *Phys. Rev. B* **93**, 195147 (2016).
- [61] Madhuparna Karmakar and Pinaki Majumdar, “Thermally induced gaplessness and fermi arcs in a “ $s$ -wave” magnetic superconductor,” (2018), 10.48550/ARXIV.1808.02012.
- [62] A. I. Buzdin, “Proximity effects in superconductor-ferromagnet heterostructures,” *Rev. Mod. Phys.* **77**, 935–976 (2005).
- [63] Etienne Boaknin, R. W. Hill, Cyril Proust, C. Lupien, Louis Taillefer, and P. C. Canfield, “Highly anisotropic gap function in borocarbide superconductor LuNi<sub>2</sub>B<sub>2</sub>C,” *Phys. Rev. Lett.* **87**, 237001 (2001).
- [64] Tadataka Watanabe, Minoru Nohara, Tetsuo Hanaguri, and Hidenori Takagi, “Anisotropy of the superconducting gap of the borocarbide superconductor YNi<sub>2</sub>B<sub>2</sub>C with ultrasonic attenuation,” *Phys. Rev. Lett.* **92**, 147002 (2004).
- [65] T. Baba, T. Yokoya, S. Tsuda, T. Watanabe, M. Nohara, H. Takagi, T. Oguchi, and S. Shin, “Angle-resolved photoemission observation of the superconducting-gap minimum and its relation to the nesting vector in the phonon-mediated superconductor YNi<sub>2</sub>B<sub>2</sub>C,” *Phys. Rev. B* **81**, 180509 (2010).
- [66] In-Sang Yang, M. V. Klein, S. L. Cooper, P. C. Canfield, B. K. Cho, and Sung-Ik Lee, “Study of the superconducting gap in RNi<sub>2</sub>B<sub>2</sub>C ( $r = Y, Lu$ ) single crystals by inelastic light scattering,” *Phys. Rev. B* **62**, 1291–1295 (2000).
- [67] T. Yokoya, T. Kiss, T. Watanabe, S. Shin, M. Nohara, H. Takagi, and T. Oguchi, “Ultrahigh-resolution photoemission spectroscopy of ni borocarbides: Direct observation of the superconducting gap and a change in gap anisotropy by impurity,” *Phys. Rev. Lett.* **85**, 4952–4955 (2000).

## Supplementary Material: Temperature tuned Fermi surface topology and segmentation in non-centrosymmetric superconductors

### METHOD AND INDICATORS

#### Path integral formalism and Static Path Approximation (SPA)

The attractive Hubbard model on a 2D square lattice with RSOC and in-plane Zeeman field along the  $x$ -axis reads as,

$$H = - \sum_{\langle ij \rangle, \sigma} t_{ij} (c_{i,\sigma}^\dagger c_{j,\sigma} + h.c.) - \mu \sum_{i,\sigma} \hat{n}_{i,\sigma} + \lambda \sum_{ij,\sigma,\sigma'} (c_{i,\sigma}^\dagger (i\hat{\sigma}_y)_{\sigma,\sigma'} c_{j,\sigma'} + c_{i,\sigma}^\dagger (-i\hat{\sigma}_x)_{\sigma,\sigma'} c_{j,\sigma'}) + h \sum_i (c_{i,\uparrow}^\dagger c_{i,\downarrow} + c_{i,\downarrow}^\dagger c_{i,\uparrow}) - |U| \sum_i \hat{n}_{i,\uparrow} \hat{n}_{i,\downarrow} \quad (S1)$$

where,  $t_{ij} = t = 1$  is the amplitude of nearest neighbor hopping and sets the energy scale of the problem.  $\lambda$  is the strength of RSOC and  $\mu$  is the global chemical potential.  $|U| > 0$  is the onsite Hubbard interaction. In terms of the Grassmann fields  $\psi_{i,\sigma}(\tau)$  and  $\bar{\psi}_{i,\sigma}(\tau)$  we write the Hubbard partition function as,

$$Z = \int \mathcal{D}\psi \mathcal{D}\bar{\psi} e^{-S[\psi, \bar{\psi}]} \quad (S2)$$

where,

$$S = \int_0^\beta d\tau [ \sum_{ij,\sigma,\sigma'} \{ \bar{\psi}_{i,\sigma} ((\partial_\tau - \mu)\delta_{ij} - t_{ij}) \psi_{j,\sigma} \} + \lambda \sum_{ij,\sigma,\sigma'} ( \bar{\psi}_{i,\sigma} (i\hat{\sigma}_y)_{\sigma,\sigma'} \psi_{j,\sigma'} + \bar{\psi}_{i,\sigma} (-i\hat{\sigma}_x)_{\sigma,\sigma'} \psi_{j,\sigma'} ) - |U| \sum_{i,\sigma,\sigma'} \bar{\psi}_{i,\sigma} \psi_{i,\sigma} \bar{\psi}_{i,\sigma'} \psi_{i,\sigma'} + h \sum_{i,\sigma,\sigma'} \bar{\psi}_{i,\sigma} (\hat{\sigma}_x)_{\sigma,\sigma'} \psi_{i,\sigma'} ] \quad (S3)$$

The interaction generates a quartic term in  $\psi$  which can not be readily evaluated. In order to make the model numerically tractable we decouple the quartic interaction exactly using Hubbard Stratonovich decomposition [44, 45]. The decomposition introduces the complex scalar bosonic auxiliary fields  $\Delta_i(\tau)$  and  $\Delta_i^*(\tau)$  which couples to the SC pairing. The corresponding partition function reads as,

$$Z = \int \mathcal{D}\Delta \mathcal{D}\Delta^* \mathcal{D}\psi \mathcal{D}\bar{\psi} e^{-S_1[\psi, \bar{\psi}, \Delta, \Delta^*]} \quad (S4)$$



where, the action is defined as,

$$S_1 = \int_0^\beta d\tau \left[ \sum_{ij,\sigma,\sigma'} \{ \bar{\psi}_{i,\sigma} ((\partial_\tau - \mu) \delta_{ij} t_{ij}) \psi_{j,\sigma} \} + \lambda \sum_{ij,\sigma,\sigma'} (\bar{\psi}_{i,\sigma} (i\hat{\sigma}_y)_{\sigma,\sigma'} \psi_{j,\sigma'} + \bar{\psi}_{i,\sigma} (-i\hat{\sigma}_x)_{\sigma,\sigma'} \psi_{j,\sigma'}) \right. \\ \left. + \sum_i (\Delta_i(\tau) \bar{\psi}_{i,\uparrow} \bar{\psi}_{i,\downarrow} + \Delta_i^*(\tau) \psi_{i,\downarrow} \psi_{i,\uparrow}) + \frac{|\Delta_i(\tau)|^2}{|U|} \right] + h \sum_{i,\sigma,\sigma'} \bar{\psi}_{i,\sigma} (\hat{\sigma}_x)_{\sigma,\sigma'} \psi_{i,\sigma'} \quad (S5)$$

The  $\psi$  integral is now quadratic but at the cost of additional integration over  $\Delta_i(\tau)$  and  $\Delta_i^*(\tau)$ . The weight factor for the  $\Delta_i$  configurations can be determined by integrating out the  $\psi$  and  $\bar{\psi}$  and using these weighted configurations one goes back and computes the fermionic properties. Formally,

$$Z = \int \mathcal{D}\Delta \mathcal{D}\Delta^* e^{-S_2[\Delta, \Delta^*]} \quad (S6)$$

where,

$$S_2 = \ln[\text{Det}[\mathcal{G}^{-1} - \Delta_i(\tau)]] + \frac{|\Delta_i(\tau)|^2}{|U|} \quad (S7)$$

where,  $\mathcal{G}$  is the electron Greens function in the  $\{\Delta_i\}$  background. The weight factor for an arbitrary space-time configuration  $\Delta_i(\tau)$  involves the determination of the fermionic determinant in that background.

In terms of the Matsubara modes we can write the bosonic auxiliary field as  $\Delta_i(\Omega_n)$ . Within the purview of SPA we retain only the  $\Omega_n = 0$  modes of the auxiliary fields, such that  $\Delta_i(\Omega_n) \rightarrow \Delta_i$ . Thus, we take into account the spatial fluctuations in  $\Delta_i$  at all orders but retain only the zero mode in the Matsubara frequency. The SPA reduces to BdG-MFT at  $T = 0$ , while at  $T \neq 0$  we retain not just the saddle point configuration but “all configurations” based on the weight factor  $e^{-S_2}$  above. Inclusion of the classical fluctuations on amplitude and phase suppresses the SC order quicker than the MFT and allows the determination of the thermal scales with quantitative accuracy [46–49].

### Monte Carlo simulation

The random background configurations of  $\{\Delta_i\}$  are generated numerically via Monte Carlo simulation and obeys the Boltzmann distribution,

$$P\{\Delta_i\} \propto \text{Tr}_{c,c^\dagger} e^{-\beta H_{eff}} \quad (S8)$$

where, the effective Hamiltonian  $H_{eff}$  reads as,

$$H_{eff} = -t \sum_{\langle ij \rangle, \sigma} (c_{i,\sigma}^\dagger c_{j,\sigma} + H.c.) - \mu \sum_{i,\sigma} \hat{n}_{i,\sigma} + \lambda \sum_{ij,\sigma,\sigma'} (c_{i,\sigma}^\dagger (i\hat{\sigma}_y)_{\sigma,\sigma'} c_{j,\sigma'} + c_{i,\sigma}^\dagger (-i\hat{\sigma}_x)_{\sigma,\sigma'} c_{j,\sigma'}) \\ + \sum_i (\Delta_i c_{i,\uparrow}^\dagger c_{i,\downarrow}^\dagger + \Delta_i^* c_{i,\downarrow} c_{i,\uparrow}) + \sum_i \frac{|\Delta_i|^2}{|U|} + h \sum_{i,\sigma,\sigma'} c_{i,\sigma}^\dagger (\hat{\sigma}_x)_{\sigma,\sigma'} c_{i,\sigma'} \quad (S9)$$

For large and random configurations the trace is computed numerically, wherein  $H_{eff}$  is diagonalized for each attempted update of  $\Delta_i$  and converge to the equilibrium configuration via Metropolis algorithm. The process is numerically expensive and involves a computation cost of  $\mathcal{O}(N^3)$  per update (where  $N = L \times L$  is the number of lattice sites), thus the cost per MC sweep is  $\sim N^4$ . The computation cost is cut down by using a traveling cluster algorithm (TCA), wherein instead of diagonalizing the entire Hamiltonian for each attempted update of  $\Delta_i$ , we diagonalize a smaller cluster of size  $N_c \times N_c$  surrounding the update site. The corresponding computation cost now scales as  $\mathcal{O}(NN_c^3)$  which is linear in  $N$ . This allows us to access larger system size with reasonable computation cost. The equilibrium configurations obtained via the combination of MC and Metropolis at different temperatures are used to determine the fermionic correlators [46–49].

### Bogoliubov-de-Gennes mean field theory

We have used BdG-MFT as an alternate scheme to calculate the ground state properties of the system. The use of MFT allows us to access large system sizes and our ground state calculations are carried out on a system size of  $L = 70$ . The free energy minimization scheme involves optimization over trial solutions w. r. t.  $|\Delta_i|$  and  $\mathbf{q}$ , where  $|\Delta_i|$  is real and  $|\Delta_{\mathbf{q}}| = \Delta_0$

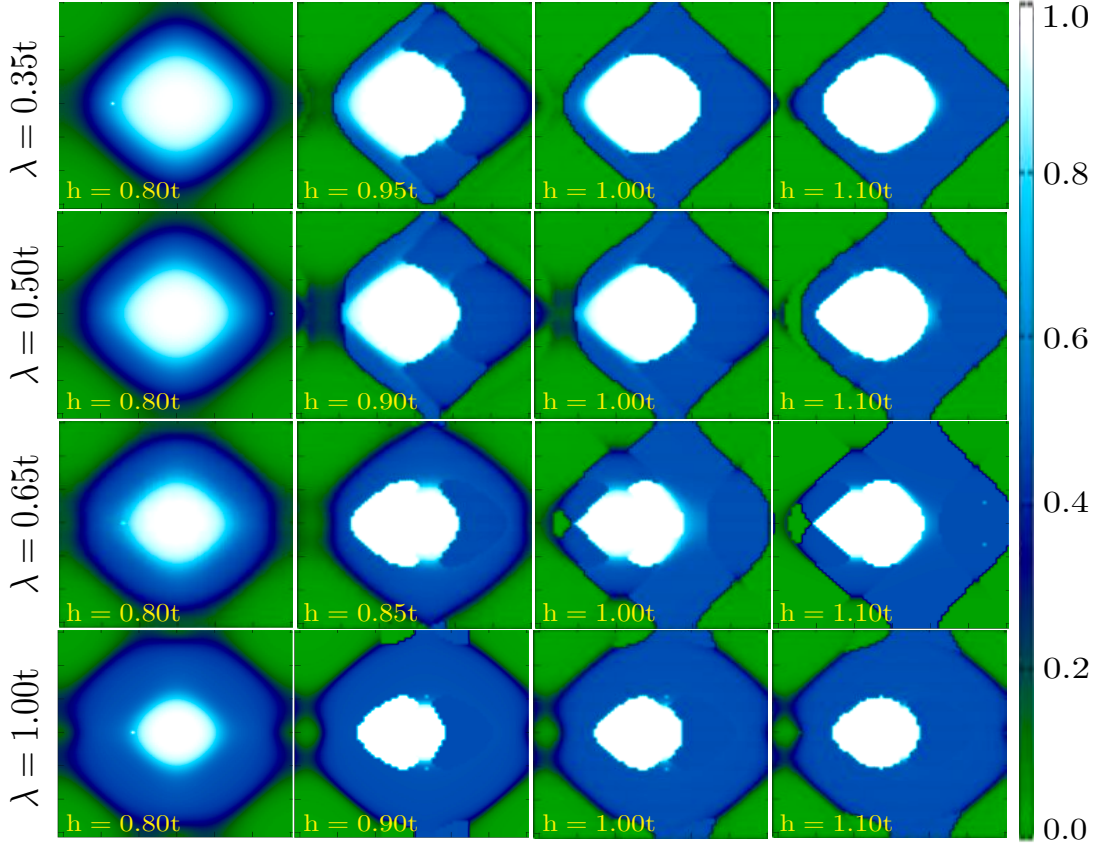


FIG. S1. Evolution of the Fermi surface with in-plane Zeeman field ( $h$ ) for selected RSOC ( $\lambda$ ). Note the topological transition (TT) at intermediate  $\lambda - h$  cross sections, wherein a single self intersecting FS is realized. Zeeman effect dominates at strong  $\lambda$ , with significant mismatch in the size of the FSs. The calculations are carried out using BdG-MFT for a system size of  $L = 70$ .

corresponds to the amplitude of the uniform SC state. For the FFLO phase we choose different trial solutions corresponding to the, (i) uniaxial modulation  $\Delta_i \propto \Delta_0 \cos(qx_i)$ , (ii) 2D modulation  $\Delta_i \propto \Delta_0 (\cos(qx_i) + \cos(qy_i))$  and (iii) diagonal modulation  $\Delta_i \propto \Delta_0 \cos[q(x_i + y_i)]$ . For the helical SC phase the trial solution is defined as,  $\Delta_i \propto \Delta_0 e^{i\mathbf{q} \cdot \mathbf{r}_i}$ . We work in the grand canonical ensemble and for  $\mu \in [0 : -4]$  with  $\delta\mu = 0.5$  the free energy optimization is carried out for different  $\lambda$  and  $h \in [0 : 1.5]$ , in each case. Irrespective of the choice of  $\lambda$  the low magnetic field regime  $h \leq h_{c1}$  hosts an uniform SC phase with  $\mathbf{q} = 0$ . Over the regime  $h_{c1} < h \leq h_{c2}$  a stable helical SC phase is realized, except close to  $\mu \sim 0$ , where a FFLO phase is stabilized for certain choices of  $\lambda$ . The  $\mu$  dependence of  $h_{c1}$  and  $h_{c2}$  is weakly non monotonic, with an increase in the regime  $0 < \mu \leq -t$ , followed by a monotonic reduction for  $-t < \mu \leq -4t$ . The choice of  $\mu = -t$  for the results presented in the main text is dictated by the maximum  $h_{c2}$  at this chemical potential, which allows a wider regime of helical SC state.

### Indicators

The various phases of the system are characterized based on the following indicators,

- (1) Pairing field structure factor,

$$S(\mathbf{q}) = \frac{1}{N^2} \sum_{ij} \langle \Delta_i \Delta_j^* \rangle e^{i\mathbf{q} \cdot (\mathbf{r}_i - \mathbf{r}_j)} \quad (\text{S10})$$

where,  $N = L \times L$  is the number of lattice sites.

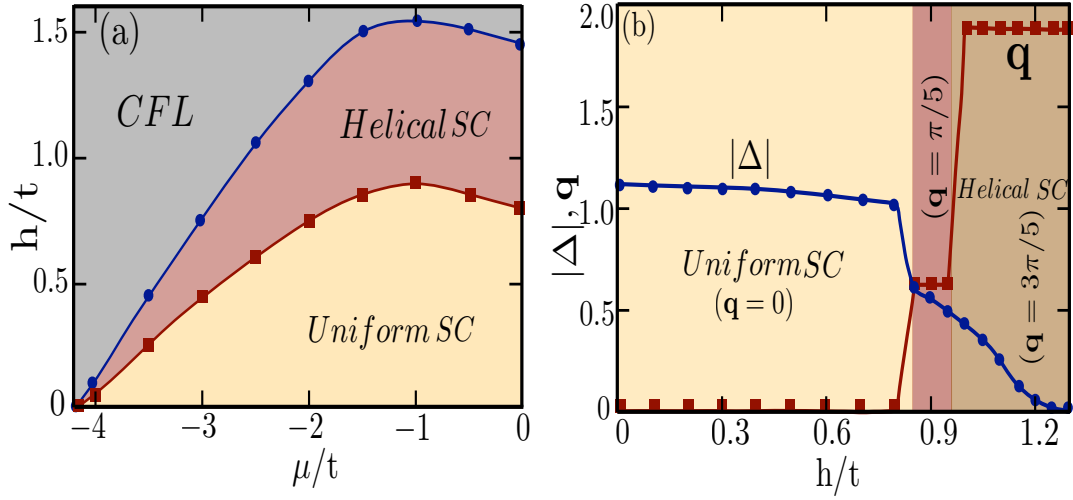


FIG. S2. (a) Ground state phase diagram in the  $\mu - h$  plane for the selected RSOC of  $\lambda = 0.65t$ . The thermodynamic phases include uniform and helical SC phases with the corresponding critical fields  $h_{c1}$  and  $h_{c2}$ , respectively. (b) Zeeman field dependence of average superconducting pairing field amplitude ( $|\Delta|$ ) and pairing momentum ( $\mathbf{q}$ ), at  $\lambda = 0.65t$ , in the ground state. The first order transition between the uniform and helical SC phases is signaled by the sharp discontinuity in  $|\Delta|$  and  $\mathbf{q}$ . The helical phase comprises of uniaxial modulations with the pairing momenta being  $(0, \pi/5)$  and  $(0, 3\pi/5)$ .

(2) Single particle density of states (DOS),

$$N(\omega) = \frac{1}{N} \langle \sum_{i,n} (|u_n^i|^2 \delta(\omega - E_n) + |v_n^i|^2 \delta(\omega + E_n)) \rangle \quad (\text{S11})$$

where,  $u_n^i$  and  $v_n^i$  are the Bogoliubov-de-Gennes (BdG) eigenvectors corresponding to the eigenvalue  $E_n$ .

(3) Spectral function,

$$A(\mathbf{k}, \omega) = -(1/\pi) \text{Im } G(\mathbf{k}, \omega) \quad (\text{S12})$$

here,  $G(\mathbf{k}, \omega) = \lim_{\delta \rightarrow 0} G(\mathbf{k}, i\omega_n)|_{i\omega_n \rightarrow \omega + i\delta}$ , with,  $G(\mathbf{k}, i\omega_n)$  being the imaginary frequency transform of  $\langle c_{\mathbf{k}}(\tau) c_{\mathbf{k}}^\dagger(0) \rangle$ .

(4) Low energy spectral weight distribution,

$$A(\mathbf{k}, 0) = -(-1/\pi) \text{Im } G(\mathbf{k}, 0) \quad (\text{S13})$$

(5) Momentum resolved fermionic occupation number,

$$n(\mathbf{k}) = \sum_{\sigma} \langle c_{\mathbf{k},\sigma}^\dagger c_{\mathbf{k},\sigma} \rangle \quad (\text{S14})$$

### EFFECT OF SOC:- FERMI SURFACE EVOLUTION

We show the RSOC dependence of FS topology in Fig.S1. For  $h > h_{c1}$  a helical SC state with finite- $q$  pairing is realized for weak and intermediate RSOC. For strong RSOC the Zeeman effect dominates and there is significant mismatch in the size of the helical FSs; superconductivity is strongly suppressed in this regime. The topological transition (TT) between the inter and intraband helical SC pairing is most prominent over the regime of intermediate RSOC ( $\lambda = 0.50t$  and  $\lambda = 0.65t$ ). The TT can thus be controlled by suitably tuning the combination of RSOC strength and the in-plane Zeeman field.

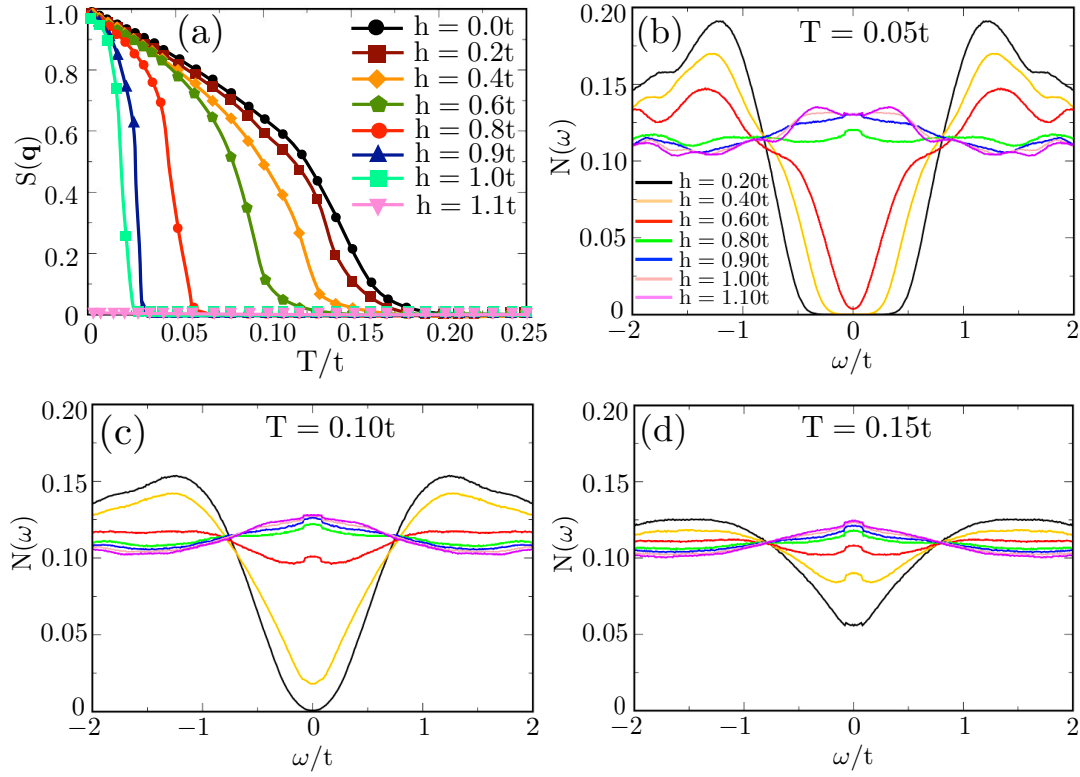


FIG. S3. (a) Temperature dependence of the pairing field structure factor ( $S(\mathbf{q})$ ) at  $\lambda = 0.65t$  and different Zeeman field. The point of inflection of each curve corresponds to the respective  $T_c$ . (b)-(c) Zeeman field dependence of the single particle DOS at the Fermi level for the selected temperatures of  $T = 0.05t$ ,  $T = 0.10t$  and  $T = 0.15t$ , respectively.

## GROUND STATE

We map out the ground state phase diagram of the system in the  $\mu - h$  plane at  $\lambda = 0.65t$ , in Fig.S2(a). The regimes of  $\mathbf{q} = 0$  and  $\mathbf{q} \neq 0$  pairing are demarcated as the uniform and helical SC states, respectively. RSOC stabilizes a helical SC state over the entire  $\mu$  regime, unlike the situation in the absence of RSOC where application of an in-plane Zeeman field gives rise to an amplitude modulated FFLO state [46]. For the rest of our calculations we have fixed  $\mu = -t$ , corresponding to an electron number density of  $n \approx 0.75t$ .

In Fig.S2(b) we show the behavior of the mean pairing field amplitude  $|\Delta| = \langle |\Delta_i| \rangle$  and the pairing momentum  $\mathbf{q}$ , at  $\mu = -t$  and  $\lambda = 0.65t$ . Over the uniform SC regime ( $0 < h \leq h_{c1}$ ) the  $|\Delta|$  is nearly constant and the corresponding pairing momentum is at  $\mathbf{q} = 0$ . At  $h = h_{c1}$  the system undergoes a first order transition to the helical SC state, accompanied by a strong suppression in the pairing field amplitude. Concomitantly, the pairing momentum becomes finite with  $\mathbf{q} \neq 0$ . While  $|\Delta|$  undergoes continuous suppression with  $h$ , the pairing momenta remains largely constant over the regime  $h_{c1} < h \leq h_{tp}$ . The topological transition between the inter and intraband helical SC states at  $h_{tp}$  is accompanied by yet another first order transition, as suggested by the discontinuity in the pairing momenta  $\mathbf{q}$ . The jump discontinuity of  $\mathbf{q}$  across the topological transition to a single self intersecting FS has been recently discussed within the purview of MFT [37]. Note that this topological transition can not be detected via real space signatures and standard experimental probes quantifying the SC transitions.

## DETERMINATION OF THE THERMAL SCALES

The transition temperature ( $T_c$ ) corresponding to the loss of (quasi) long range SC phase coherence, shown in the main text, is determined based on the temperature dependence of the pairing field structure factor ( $S(\mathbf{q})$ ). We show the same in Fig.S3(a) as function of the Zeeman field. The point of inflection of each curve correspond to the respective  $T_c$ . The Zeeman field strongly suppresses the  $T_c$  and at  $h \sim h_{c1}$  a first order transition between the uniform and the helical SC phases is realized. Within the



helical SC phase ( $h_{c1} < h \leq h_{c2}$ ) the  $S(\mathbf{q})$  changes with the Zeeman field via consecutive first order transitions. The system loses SC order at  $h \sim h_{c2}$ , as signaled by the vanishing  $S(\mathbf{q})$ .

In Fig.S3(b)-(d) we show the field dependence of the single particle DOS at the Fermi level at three different thermal cross sections. At  $T = 0.05t$  (Fig.S3(b)) the system is a gapped uniform superconductor at  $h = 0.2t$  with a robust spectral gap at the Fermi level. Increasing  $h$  suppresses the gap progressively as observed at  $h = 0.4t$  and finally leads to its closure at  $h = 0.6t$ , indicated by a finite spectral weight at the Fermi level.  $h = 0.6t$  corresponds to a gapless SC state (see Fig.1(a) in the main text) with (quasi) long range SC phase coherence indicated by the broadened but prominent QP peaks at the gap edges. The system undergoes transition to a regime with helical SC correlations at  $h \geq 0.9t$ , characterized by a gapless spectra and thermally diffused signatures of in-gap states. Zeeman field progressively suppresses the in-gap states and at  $h \sim 1.1t$  the spectra is featureless, corresponding to a magnetic metal.

At  $T = 0.10t$  (Fig.S3(c)) the system is a uniform SC with suppressed spectral gap at  $h = 0.2t$  and a gapless superconductor at  $h = 0.4t$ . A change in the FS topology with the shift in the Dirac point to  $\mathbf{k} \neq 0$  takes place for  $h = 0.6t$  at  $T = 0.10t$  (see Fig.1(a) of the main text). The corresponding single particle DOS shows a sudden large spectral weight accumulation at the Fermi level which we attribute to the short range helical SC correlations. The coherence peaks at the gap edges are strongly suppressed via transfer of spectral weight away from the Fermi level. Further increase in  $h$  progressively accumulates the spectral weight at the Fermi level as the system crosses over to the pseudogap phase and eventually to the CFL. The  $T = 0.15t$  (Fig.S3(d)) cross section corresponds to a gapless superconductor at low  $h$ , which progressively gives way to the pseudogap and then to the CFL phases via spectral weight accumulation at the Fermi level.